# Low Prandtl number fluid convection modelled using symbolic algebra (REDUCE) and Matlab

Tim Passmore[*] A. J. Roberts[†]

(Received 7 July 2001)

## Abstract

Using the Boussinesq approximation for a fluid of low Prandtl number, a low dimensional model of the onset of Rayleigh-Benard convection is developed. The initial roll mode instability is considered for a fluid, heated from below, between parallel, horizontal, non-slip, constant-temperature boundaries. Centre manifold theory provides a way of constructing a low dimensional model of the resulting two dimensional flow. Computer algebra implemented in REDUCE is used to symbolically expand the centre manifold as an asymptotic series in the convective amplitude. The spatial

---

[*] Dept. Maths & Computing, University of Southern Queensland, Toowoomba, 4350, AUSTRALIA. mailto:passmore@usq.edu.au

[†] Dept. Maths & Computing, University of Southern Queensland, Toowoomba, 4350, AUSTRALIA. mailto:aroberts@usq.edu.au

[0] See http://anziamj.austms.org.au/V44/CTAC2001/Pass for this article, © Austral. Mathematical Soc. 2003. Published 1 April 2003. ISSN 1446-8735

structure functions in this expansion are then found numerically in Matlab. A feature of this approach is that code output from REDUCE is used, with only minor syntactic editing, as the Matlab code to perform the numerical iteration. Thus a coding task which would have been difficult by hand is easily automated. The technique is generally applicable to perturbation expansions and its computational advantages over more formal Galerkin type expansions are discussed.

# Contents

# 1 Introduction

The onset of Rayleigh-Bénard convection illustrates behaviour that is typical of many physical systems governed by nonlinear partial differential equations, as they undergo a bifurcation. The challenges it presents to the mathematical modeller are also typical. It is necessary to develop model equations which are of low enough dimension to be tractable and yet still able to capture the dynamics of interest. Centre manifold theory provides a systematic way of doing this which does not rely on heuristic arguments [20, 21].

Sufficiently close to the bifurcation point, a local analysis based on some form of perturbation expansion provides useful approximate solutions. Ideally, such an expansion should be capable of being extended to higher order, if necessary, to provide better approximations. In practice, for example with formal Galerkin type expansions [8, 12], it is often difficult to compute more than the first few terms in the expansion and these may not provide sufficient accuracy. It is not the algebraic structure of the higher order terms which makes them difficult to compute, but their increasingly convoluted dependence on spatial variables [12].

Rayleigh-Bénard convection has been extensively studied both experimentally and theoretically (for recent reviews see [3, 10]). A fluid is confined between horizontal, non-slip boundaries, here assumed to have infinite horizontal extent. Heat is applied from below in such a way that each boundary has a constant temperature, with the temperature of the lower boundary being greater than the upper

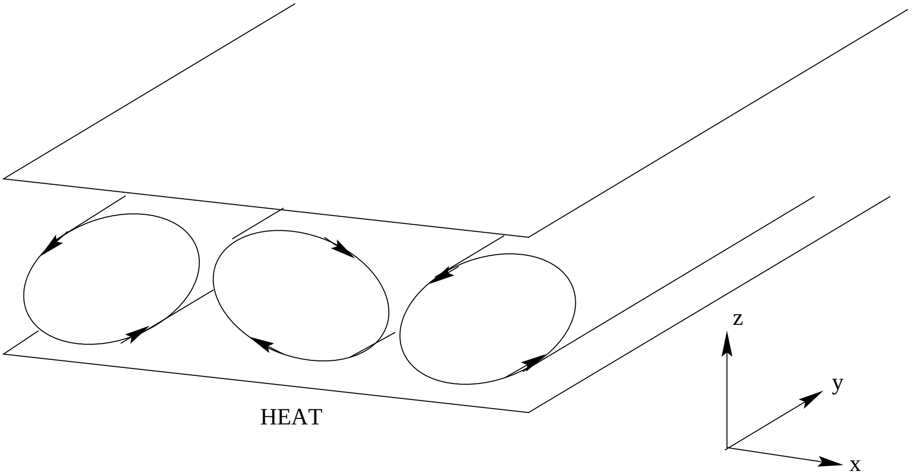

Figure 1: Schematic diagram of convective rolls.

boundary.

We assume that density variations within the fluid are only considered significant if they are multiplied by the gravitational acceleration, $g$, and all other material properties are assumed constant, which is called the Boussinesq approximation [5]. Consider such a fluid, initially at rest and transmitting heat only by conduction. As noted by Rayleigh [19], if the temperature difference between the lower and upper boundaries is increased, the fluid will eventually become unstable. This buoyancy driven instability leads, in the first instance, to a convection pattern of parallel cylindrical rolls of moving fluid, see Figure 1.

Experimentally, quasi-Boussinesq conditions for Rayleigh-Bénard convection have been achieved in high pressure gases [9]. Gas-convection cells can be constructed with aspect ratios greater than 100 [16, 1], and allow visualisation of the horizontal, convective planform by the shadowgraph technique [11]. In such cells ideal straight roll convection patterns can be generated and studied.

The Prandtl number of pure gases are typically low ($\sigma \approx 1$), but by using mixtures of gases, a range of Prandtl numbers from $0{\cdot}17 < \sigma < 115$ is achievable [14, 3]. The low Prandtl number regime ($\sigma \lesssim 1$) has been of particular interest since the discovery of spiral-defect chaos [16, 17], which is a competing stable attractor with ideal straight rolls in the same parameter regime [6, 2]. This competition is mediated by mean-flow effects due to roll curvature [23, 3]. It is important therefore, to develop models of Rayleigh-Bénard convection which can incorporate these mean-flow effects, and we construct such a model here.

From the equations of motion for the fluid (see §2) we show, in §3, that spatially periodic solutions of the full system settle exponentially quickly onto a six-dimensional centre manifold, $\mathcal{M}_0$, and show how to compute $\mathcal{M}_0$ by iteration. Dynamical variables are expanded asymptotically in terms of the amplitude of roll mode convection (see §§3.1). Solutions are assumed to be periodic in the horizontal, $x$ direction. In the vertical, $z$ direction, the spatial dependence of each term in the expansion is given by a structure function to be determined.

In §4 the computation of the vertical structure functions is done in two steps. Firstly, with the aid of the computer algebra package REDUCE, the asymptotic expansions are truncated to the desired order and substituted into the Navier Stokes equations (see §§4.1). REDUCE computes the nonlinear expression for the residual of each term in the expansion, a task which one would not contemplate doing by hand. These residual expressions are then output by REDUCE in a form which, with minor syntactic editing, becomes a MATLAB m-file. In the second step, the iteration equations are discretised in MATLAB using finite differences and the structure functions are computed numerically by iteration (see §§4.2).

This two-step process decouples the algebraic approximation and the numerical approximation. If truncation to a different order is required, the REDUCE code must be rerun and a new m-file prepared. If a finer numerical grid is required, MATLAB iterations must be rerun. The effect of both types of approximation on the solution can be independently tested. However, the main advantage is that high-order expansions are computed relatively easily. Structure functions are computed for expansions truncated to 36, 80, 81 and 180 terms and their corresponding solutions compared. Analytic techniques like the Galerkin method might be expected to yield four or five terms at best [15, Section 2.4].

Lastly, in §5, truncation errors are estimated and some indication of useful parameter ranges are given.

## 2 Equations of motion for a low Prandtl number fluid

Define Cartesian coordinates $x$ horizontal and $z$ vertical with non-slip boundaries at $z = 0$ and $z = d$ (see Figure 1). We assume that the cylindrical convective rolls run parallel to the $y$ axis and model the flow in the $xz$-plane.

The equations of motion for a Newtonian, incompressible, Boussinesq fluid (see for example [15]) are:

$$\begin{aligned}
\frac{\partial\theta}{\partial t} + \mathbf{u}\cdot\nabla\theta &= \kappa\nabla^2\theta + \beta\mathbf{u}\cdot\hat{\mathbf{z}}\,, \\
\frac{\partial\mathbf{u}}{\partial t} + \mathbf{u}\cdot\nabla\mathbf{u} &= -\frac{1}{\rho_0}\nabla p + \nu\nabla^2\mathbf{u} + \alpha g\theta\hat{\mathbf{z}}\,,
\end{aligned} \qquad (1)$$

$$\nabla \cdot \mathbf{u} = 0 ,$$

where $\mathbf{u}$ is the fluid velocity field and $\rho$ is the density field. $\theta$ and $p$ are, respectively, corrections to the static temperature and pressure fields: $T = T_0 - \beta z + \theta$, and $P = P_0 - \rho_0 g(z + \alpha\beta z^2/2) + p$. The thermal $\kappa$, kinematic viscosity $\nu$, gravitational acceleration $g$, and volume coefficient of thermal expansion $\alpha$, are all assumed constant.

## 2.1 Non-dimensional equations of motion

We construct a scaling of (1) to obtain non-dimensional equations of motion appropriate to low Prandtl number fluids. Scale lengths with $d/\pi$, pressure with $\rho_0 \nu^2 \pi^2 / d^2$, density with $\rho_0$ and scale temperature changes with $\beta d \sigma / \pi R$. At low Prandtl number it is best to use the viscous diffusion time, $d^2/\pi^2 \nu$, to scale time, rather than the thermal diffusion time [4, 15, §1.4]. The non-dimensional equations of motion are

$$\begin{aligned}
\sigma \left( \frac{\partial \theta}{\partial t} + \mathbf{u} \cdot \nabla \theta \right) &= \nabla^2 \theta + R w , \\
\frac{\partial \mathbf{u}}{\partial t} + \mathbf{u} \cdot \nabla \mathbf{u} + \nabla p &= \nabla^2 \mathbf{u} + \theta \hat{\mathbf{z}} , \\
\nabla \cdot \mathbf{u} &= 0 .
\end{aligned} \tag{2}$$

The parameters $\sigma$ and $R$ are the Prandtl and Rayleigh numbers respectively,

$$\sigma = \frac{\nu}{\kappa} \quad \text{and} \quad R = \frac{g \alpha \beta d^4}{\kappa \nu \pi^4} .$$

Note that the length scaling has been chosen so that the vertical boundaries now lie at $z = 0$ and $z = \pi$. Constant temperature, non-slip boundaries give boundary conditions

$$u = w = \theta = 0 , \quad \text{on } z = 0, \pi . \tag{3}$$

## 2.2 Linear stability analysis

Consider a hot droplet ($\theta > 0$) at a higher temperature than surrounding fluid, which has an undisturbed, static temperature profile. Since the density of the droplet decreases with temperature, it is less dense than surrounding fluid and experiences an upward buoyancy force. The fluid is heated from below, so as the droplet moves upward it encounters fluid which is even colder and more dense, the upthrust is amplified and the droplet moves higher still. However, counteracting the buoyancy force are two dissipative processes, viscous drag which tends to slow the droplet down and thermal diffusion which causes the warmer droplet to lose heat to surrounding cooler fluid, reducing the buoyancy force.

The instability develops only if the droplet is accelerated sufficiently to overcome the stabilizing effect of the dissipative processes. The conditions under which this will occur are found by linearising (2). In the low Prandtl number regime we use $\sigma$ itself as a perturbation parameter. This means that the term, $\sigma(\partial\theta/\partial t + \mathbf{u}\cdot\nabla\theta)$, in (2) is formally nonlinear and disregarded in the linear analysis since its contribution is small. Setting $\mathbf{u} = (u, 0, w)$, the linearised equations are

$$\begin{aligned} w_t &= w_{xx} + w_{zz} - p_z + \theta\,, \\ u_t &= u_{xx} + u_{zz} - p_x\,, \\ 0 &= \theta_{xx} + \theta_{zz} + Rw\,, \\ 0 &= u_x + w_z\,. \end{aligned} \tag{4}$$

If solutions have exponential time dependence, $e^{\lambda t}$, then perturbations to the initial static conduction state become unstable and grow if $\Re\lambda > 0$. The principle of *exchange of stabilities* [4], says that $\lambda$ crosses 0 with zero imaginary part. If $\lambda = 0$, the marginal

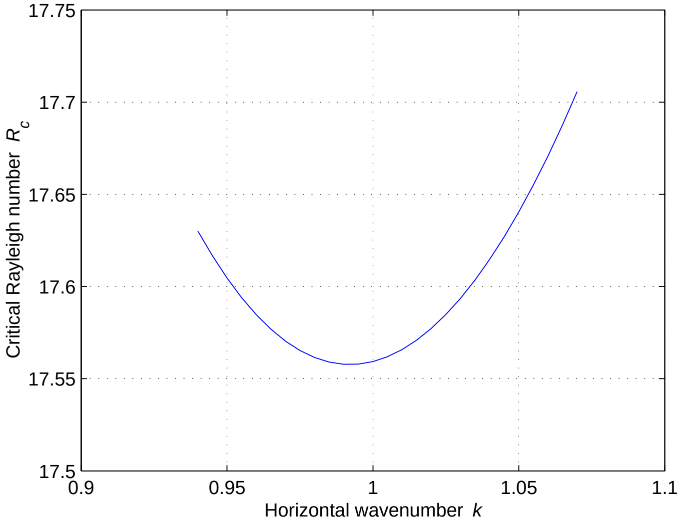

Figure 2: The marginal stability curve—below this line perturbations with horizontal wavenumber $k$ are stable with negative growth rate. Above the line perturbations are unstable and grow in amplitude.

stability case, then (4) reduces to a generalised eigenvalue problem for the critical Rayleigh number $R_c$. Assume perturbations are horizontally periodic and solve this numerically to generate the marginal stability curve shown in Figure 2. The minimum point on this curve represents the earliest possible onset of roll mode convection, at critical wavenumber $k_c$ and critical Rayleigh number[1] $R_c$:

$$k_c = 0{\cdot}9904 \quad \text{and} \quad R_c = 17{\cdot}5576\,. \tag{5}$$

---

[1] The value more usually quoted [3, 15, 5, for example], $R_c \approx 1708$, is for horizontal boundaries at $z = 0, 1$. Our scaling to $z = 0, \pi$ reduces this by a factor of $\pi^4$.

$R > R_c$ is a sufficient condition for the onset of Rayleigh-Bénard roll mode convection, but how do we model the actual flow that takes place?

# 3 Centre manifold theory yields a low dimensional model

In this section, we show how centre manifold theory provides a rigorous basis for constructing a low-dimensional model of the system. Suppose that the linearised dynamics of a system near a fixed point consists of eigenmodes which are either ‘slow’ or strongly stable. Slow modes have growth rates close to zero while strongly stable modes have large negative growth rates. The two groups are separated by a spectral gap, measured by the maximum moduli of their eigenvalues. Provided there is a sufficiently large spectral gap, between the slow modes and the stable modes, the stable modes become slaved to the slow modes and *adiabatically eliminated* from the dynamics [15, Chapter 5]. Potentially, there may be a large number of stable modes eliminated in this way, in which case the effective dynamics of the system, driven by the slow modes, is of much lower dimension.

If the slow modes are neutral, that is, their eigenvalues are either precisely zero or have zero real part, then sufficiently close to the fixed point, the dynamics of the system settle exponentially quickly onto a *centre manifold*. The stable modes quickly decay and the long-term dynamics is dominated by what happens on the centre manifold. Centre manifold theory was originally developed to answer questions about the stability of nonlinear systems. We apply it to systematically develop a low-dimensional approximation to the evolution of roll mode convection from an initially static fluid.

Useful analytic properties of centre manifolds have been summarised by Carr [7] for nonlinear dynamical systems with the properties as broadly described above.

1. A centre manifold $\mathcal{M}_0$, exists in some neighbourhood of the fixed point [7, Theorem 1].
2. The stability properties of the fixed point on $\mathcal{M}_0$ are the same as for the full system. Moreover, trajectories on $\mathcal{M}_0$ differ from trajectories of the full system only by terms $\mathcal{O}\left(e^{-\gamma t}\right)$ as $t \to \infty$, and $\gamma$ is approximately equal to the spectral gap [7, Theorem 2].
3. If solutions of the low-dimensional dynamics on $\mathcal{M}_0$ are found to some order of accuracy, then $\mathcal{M}_0$ itself is given to the same order of accuracy [7, Theorem 3].

These basic results can be generalised and extended. For instance, the assumption that the eigenvalues of the linearised problem all have non-positive real parts is not necessary [7]. Roberts has shown how to deal with a continuous spectrum near the marginal mode [20].

In fluid convection, the theory is directly applicable to the case of slowly-varying pure convective rolls—the one-dimensional planform problem. We develop this model in §§3.1, in a systematic way compared to earlier treatments which relied on heuristic arguments [22, 18]. In real convection systems with large horizontal extent there are likely to be many interacting and competing rolls. The orientation and amplitude of the rolls may vary significantly over the whole field. This leads to multi-dimensional planforms and the issue of planform selection, where the application of centre-manifold theory is problematic. Roberts [21] has shown how to solve a two-dimensional planform problem by constructing an *embedding manifold*, which embeds the centre manifold. The resulting approximations are much better than the traditional Swift-Hohenberg approximation for planform evolution.

## 3.1 Centre manifold construction

Write the linear dynamics (4) as

$$\left(\mathcal{L}(k) + B\frac{\partial}{\partial t}\right)\mathbf{V}(x,z,t) = \mathbf{0}\,, \tag{6}$$

where

$$\mathbf{V}(x,z,t) = \begin{bmatrix} w(x,z,t) \\ u(x,z,t) \\ \theta(x,z,t) \\ p(x,z,t) \end{bmatrix}, \quad \mathcal{L}(k) = \begin{bmatrix} -\nabla^2 & 0 & -I & \partial_z \\ 0 & -\nabla^2 & 0 & \partial_x \\ R & 0 & \nabla^2 & 0 \\ \partial_z & \partial_x & 0 & 0 \end{bmatrix}$$

and

$$B = \begin{bmatrix} I & 0 & 0 & 0 \\ 0 & I & 0 & 0 \\ 0 & 0 & 0 & 0 \\ 0 & 0 & 0 & 0 \end{bmatrix}.$$

$\mathcal{L}(k)$ depends on the horizontal wavenumber $k$ of the horizontally periodic solution. At $R = R_c = 17{\cdot}5576$, the eigenvalues of (6) are all negative except for $k = \pm k_c = \pm 0{\cdot}9904$, from (5), which are marginal modes ($\lambda = 0$). Thus linearly, the solution decays exponentially quickly to the roll solution

$$\mathbf{V} = a\mathbf{v}_2(z)e^{ik_cx} + b\mathbf{v}_1(z)e^{-ik_cx}\,, \tag{7}$$

where $\mathbf{v}_1(z)e^{-ik_cx}$ and $\mathbf{v}_2(z)e^{ik_cx}$ are the marginally stable eigenvectors of $\mathcal{L}(k)$, and $a$ and $b$ are the complex amplitudes of the rolls—the solution is real if and only if $b$ is the complex conjugate of $a$.

The full nonlinear equations (2), written in terms of $\mathcal{L}(k)$, meet the requirements of §3, property 1, so we are assured that a centre manifold exists. By §3, property 2, solutions on the centre manifold match solutions of (2) if we wait for exponential transients to decay.

To construct the centre manifold model, expand $\mathbf{V}(x,z,t)$ asymptotically as

$$\begin{aligned}\mathbf{V}(x,z,t) &\sim b\,\mathcal{E}^{-1}\mathbf{v}_1(z)+a\,\mathcal{E}^{1}\mathbf{v}_2(z)+b^2\,\mathcal{E}^{-2}\mathbf{v}_3(z)\\ &\quad +ab\,\mathcal{E}^{0}\mathbf{v}_4(z)+a^2\,\mathcal{E}^{2}\mathbf{v}_5(z)+\cdots\\ &\sim \sum_{n=0}^{\infty}\sum_{k=0}^{\infty}\sum_{j=1}^{\infty}\sum_{m=0}^{j}\sigma^n R_d^k a^m b^{j-m}\,\mathcal{E}^{2m-j}\mathbf{v}_l(z)\,, \end{aligned}\tag{8}$$

where we let $\mathcal{E}=e^{ik_cx}$, $R_d=R-R_c$ and $a$ and $b$ are complex amplitudes, posited to evolve slowly in time according to

$$\frac{\partial a}{\partial t}=g(a,b,R,\sigma)\,,\quad \frac{\partial b}{\partial t}=\bar g(a,b,R,\sigma)\,.\tag{9}$$

In (8), $l$ is just a convenient label consecutively numbering the coefficient functions when the terms are ordered in some consistent way. If the $k$ summation in (8) runs from $0,1,\ldots,K$, and the $j$ summation runs from $1,2,\ldots,J$, then the label $l$, labelling the $\mathbf{v}_l(z)$, is chosen to be

$$l=(n(K+1)+k)\left[\frac{J(J+3)}{2}\right]+\frac{(j-1)(j+2)}{2}+(m+1)\,.$$

The form of (8) arises from (2) where nonlinear combinations of real variables generate terms with the structure

$$(a\mathcal{E}+b\mathcal{E}^{-1})^j=\sum_{m=0}^{j}a^m b^{j-m}\mathcal{E}^{2m-j}\,.$$

These terms are also multiplied by powers of the two other perturbation parameters, $\sigma$ the Prandtl number, which is small and $R_d = R - R_c$, the difference between the Rayleigh number and critical Rayleigh number.

Likewise, $g(a, b, R, \sigma)$ is expanded asymptotically as

$$g(a, b, R, \sigma) \sim \sum_{n,k,j,m} \sigma^n R_d^k a^m b^{j-m} g_l\,, \tag{10}$$

but here only terms with $2m-j = 1$ have coefficients $g_l \neq 0$, because the evolution (9), must be invariant to an arbitrary rotation $e^{i\varphi}$ applied to the amplitude $a$. Such a rotation generates a horizontal phase shift in the flow, which is horizontally periodic. Hence the phase shift $\varphi$ should have no effect on the system dynamics.

## 3.2 Iterative scheme

To compute the nonlinear shape of the centre manifold and the evolution thereon, we seek refinements to the linear solutions:

$$\begin{aligned} w &= \tilde{w} + w'\,, & p &= \tilde{p} + p'\,, \\ u &= \tilde{u} + u'\,, & g &= \tilde{g} + g'\,, \\ \theta &= \tilde{\theta} + \theta'\,, & \bar{g} &= \tilde{\bar{g}} + \bar{g}'\,. \end{aligned}$$

These must satisfy (2), leading to

$$\begin{aligned} & g'\,\mathcal{E}^1 w_2(z) + \bar{g}'\,\mathcal{E}^{-1} w_1(z) - \nabla^2 w' - \theta' + p'_z \\ & \quad = -\tilde{w}_t - \tilde{u}\tilde{w}_x - \tilde{w}\tilde{w}_z - \tilde{p}_z + \nabla^2 \tilde{w} + \tilde{\theta}\,, \\ & g'\,\mathcal{E}^1 u_2(z) + \bar{g}'\,\mathcal{E}^{-1} u_1(z) - \nabla^2 u' + p'_x \\ & \quad = -\tilde{u}_t - \tilde{u}\tilde{u}_x - \tilde{w}\tilde{u}_z - \tilde{p}_x + \nabla^2 \tilde{u}\,, \\ & R w' + \nabla^2 \theta' = \sigma\left(\tilde{\theta}_t + \tilde{u}\tilde{\theta}_x + \tilde{w}\tilde{\theta}_z\right) - \nabla^2 \tilde{\theta} - R\tilde{w}\,, \\ & u'_x + w'_z = -\left(\tilde{u}_x + \tilde{w}_z\right)\,, \end{aligned} \tag{11}$$

where nonlinear terms involving corrections (dashed quantities) have been ignored and $\tilde{g}$ has been approximated by a linear approximation, namely 0, when it multiplies a correction. Likewise, $\tilde{w}$, $\tilde{u}$, $\tilde{p}$ and $\tilde{\theta}$ have been approximated by the linear terms from (8) when multiplied by a correction.

The time derivatives require some care, for example using (9) to evaluate

$$\begin{aligned}
\frac{\partial u}{\partial t} &= \frac{\partial u}{\partial a}\cdot g + \frac{\partial u}{\partial b}\cdot \bar{g} \\
&= \left(\frac{\partial u'}{\partial a} + \frac{\partial \tilde{u}}{\partial a}\right)(g' + \tilde{g}) + \left(\frac{\partial u'}{\partial b} + \frac{\partial \tilde{u}}{\partial b}\right)(\bar{g}' + \tilde{\bar{g}}) \\
&= \left(\frac{\partial \tilde{u}}{\partial a}\cdot \tilde{g} + \frac{\partial \tilde{u}}{\partial b}\cdot \tilde{\bar{g}}\right) + \tilde{g}\frac{\partial u'}{\partial a} + \tilde{\bar{g}}\frac{\partial u'}{\partial b} \\
&\quad + g'\frac{\partial \tilde{u}}{\partial a} + \bar{g}'\frac{\partial \tilde{u}}{\partial b} + g'\frac{\partial u'}{\partial a} + \bar{g}'\frac{\partial u'}{\partial b} \\
&\approx \frac{\partial \tilde{u}}{\partial t} + 0 + 0 + g'\frac{\partial \tilde{u}}{\partial a} + \bar{g}'\frac{\partial \tilde{u}}{\partial b} + 0 + 0\,.
\end{aligned}$$

Setting

$$\mathbf{v}_1(z) = \begin{bmatrix} w_1(z) \\ u_1(z) \\ \theta_1(z) \\ p_1(z) \end{bmatrix} \quad \text{and} \quad \mathbf{v}_2(z) = \begin{bmatrix} w_2(z) \\ u_2(z) \\ \theta_2(z) \\ p_2(z) \end{bmatrix}$$

in (7) gives

$$\frac{\partial \tilde{u}}{\partial a} = u_2(z)\mathcal{E}\,, \quad \frac{\partial \tilde{u}}{\partial b} = u_1(z)\mathcal{E}^{-1}\,,$$

whence

$$u_t \approx g' u_2(z)\mathcal{E} + \bar{g}' u_1(z)\mathcal{E}^{-1} + \tilde{u}_t\,,$$

and $w_t$ is approximated analogously, leading to (11).

## 3.3 Solvability conditions

Equation (11) is written more succinctly as

$$g'\mathcal{E}B\mathbf{v}_2(z)+\bar{g}'\mathcal{E}^{-1}B\mathbf{v}_1(z)+\mathcal{L}(k)\mathbf{V}'(x,z,t)=\mathbf{R}(\tilde{\mathbf{V}}(x,z,t)) \qquad (12)$$

where the right-hand side represents the residual calculated for an existing approximate solution, $\tilde{\mathbf{V}}(x,z,t)$ and $\mathbf{V}'(x,z,t)$ is the vector of updates to be computed. Since $\mathcal{L}(k)$ is singular for $k=k_c$—it has a single zero eigenvalue with eigenvector $\mathcal{E}\mathbf{v}_2(z)$— we incorporate an arbitrary multiple of this vector in the $g'$ term. Likewise $\mathcal{L}(k)$ is singular for $k=-k_c$, with neutral eigenvector $\mathcal{E}^{-1}\mathbf{v}_1(z)$ and we incorporate the $\bar{g}'$ term.

These terms make (12) solvable when $k=\pm k_c$. We regard $g$ and $\bar{g}$, and $a$ and $b$, as independent variables even though physical solutions require them to be complex conjugate pairs, which they are once the iteration converges. In order to solve for $g'$ and $\bar{g}'$ in these singular cases, we need an extra *solvability condition.*

Define the amplitude $a(t)$ in (8) and (9) as

$$\begin{aligned} a(t) &\equiv \frac{k_c}{\pi}\int_{-\pi/k_c}^{\pi/k_c}\frac{1}{\pi}\int_0^{\pi} w(x,z,t)\sin z\,dz\,\mathcal{E}^{-1}\,dx \\ &= \frac{k_c}{\pi}\int_{-\pi/k_c}^{\pi/k_c}\overline{w(x,z,t)\sin z}\,\mathcal{E}^{-1}\,dx \end{aligned} \qquad (13)$$

where $w(x,z,t)$ is the vertical velocity component and the over-bar represents averaging over $z$. $b$ is defined analogously as the complex conjugate of the above

$$b(t)\equiv\frac{k_c}{\pi}\int_{-\pi/k_c}^{\pi/k_c}\overline{w(x,z,t)\sin z}\,\mathcal{E}\,dx\,.$$

Thus if

$$\begin{aligned} w(x,z,t) &= b\mathcal{E}^{-1}w_1(z) + a\mathcal{E}^{1}w_2(z) \\ &\quad + b^2\mathcal{E}^{-2}w_3(z) + ab\mathcal{E}^{0}w_4(z) + a^2\mathcal{E}^{2}w_5(z) + \cdots \,, \end{aligned}$$

then

$$\int_{-\pi/k_c}^{\pi/k_c} \overline{w(x,z,t)\sin z\mathcal{E}^{-1}\,dx} = \frac{2\pi}{k_c}\overline{aw_2(z)\sin z}\,,$$

and (13) is satisfied provided $\overline{w_2(z)\sin z} = \frac{1}{2}$. Likewise, the definition for $b(t)$ requires that $\overline{w_1(z)\sin z} = \frac{1}{2}$. So a suitable solvability condition is

$$\overline{w_l(z)\sin z} = \begin{cases} \frac{1}{2}\,, & l = 1\,,2\,, \\ 0\,, & \text{otherwise}\,, \end{cases} \tag{14}$$

where the case $l = 1, 2$ serves to scale the eigenvectors $\mathbf{v}_1(z)$ and $\mathbf{v}_2(z)$, while the 'otherwise' condition says that, for terms other than $l = 1, 2$, the coefficient functions for vertical velocity must all be orthogonal to $\sin z$.

$\mathcal{L}(0)$ is also singular—its null space is spanned by $(0,0,0,1)^{\mathsf{T}}$—reflecting the fact that an arbitrary constant pressure can always be added to $p$ in any solution of (2). In this case we append the condition

$$\int_0^{\pi} p'(z)\,dz = 0\,, \tag{15}$$

to make the solution unique. Equation (15) forces the pressure updates to have a mean of zero, that is they do not contribute to the mean field drift.

The iteration equation (12) and conditions (14) and (15) provide a complete system which is solved to generate the centre manifold model of low Prandtl number convection.

# 4 Computer implementation of the solution

To get a solution to the model equations, one must find the vertical structure functions, $\mathbf{v}_l(z)$, and the coefficients $g_l$ in the asymptotic expansions (8) and (10). As discussed in §1, attempts to expand the $\mathbf{v}_l(z)$ in some formal basis were abandoned because of the difficulties of computing coefficients for more than the first few terms. Instead, we use the computer algebra package REDUCE to substitute expansions of required form directly into the right-hand side of (12). This generates expressions for term-by-term residuals with $\mathbf{v}_l(z)$ and $g_l$ still to be determined. These expressions are then output in a form which, with simple editing, becomes a MATLAB m-file. In MATLAB, the linear operator on the left-hand side of (12) is discretised and, starting with an approximate linear solution, the iteration is performed numerically.

A similar approach was used previously by Laure and Demay [13] where the symbolic algebra package MACSYMA generated FORTRAN code for a centre manifold model of Taylor-Couette flow.

## 4.1 Computer algebra implementation in REDUCE

REDUCE does the tedious substitution of asymptotic expansions for each variable into the nonlinear residuals, calculating the results and collecting terms of the same order. The residuals are then output to a file which is edited to become a MATLAB m-file.

The key step is to decide at what order in $a$, $R_d$ and $\sigma$ to truncate the asymptotic expansions. Trying to go too high in truncation order will eventually defeat REDUCE because of the combinatorial complexity of the nonlinear residuals. The program grabs all available CPU time and swap space and fails to terminate. Nonetheless truncation at quite high order is feasible. The highest order model considered in this paper is $\mathcal{O}\left(|a|^6, R_d^3, \sigma^3\right)$, which has 180 terms in the expansion.

## 4.2 The numerical iteration in MATLAB

Armed with MATLAB expressions for the term-by-term residuals, we discretise (12) on a vertical grid of $n$ points and perform the iteration numerically. For example, the MATLAB code for the first residual of the truncation error $\mathcal{O}\left(|a|^4, R_d^2, \sigma^2\right)$ model is:

```
1   r11=-kc^2*w1+h1-pad(dmf(p1,z),z)-gb(1)*w1+d2f(w1,z);
2   r21=-kc^2*u1+pad(mav(p1,z),z)*i*kc-gb(1)*u1+d2f(u1,z);
3   r31= - rc*w1 + h1*kc^2 - d2f(h1,z);
4   r41=mav(u1,z)*i*kc - dmf(w1,z);
5   bc11= - w1;
6   bc21= - u1;
7   bc31= - h1;
8   r1=[bc11(1);r11(j);bc11(n);bc21(1);r21(j);bc21(n); ...
9   bc31(1);r31(j);bc31(n);r41;0;0];
10  vd=ll(-1)\r1;
11  w1=w1+vd(1:n); u1=u1+vd(n+(1:n));
12  h1=h1+vd(2*n+(1:n)); p1=p1+vd(3*n+(1:n-1));
13  ga(1)=ga(1)+vd(4*n); gb(1)=gb(1)+vd(4*n+1);
```

This term is a $b\mathcal{E}^{-1}$ term. In lines 1–7 of the code, the four residuals of (11) are evaluated with boundary conditions. In lines 8–10, the residuals and boundary conditions are assembled into a single vector and the update vector `vd`, which is $\mathbf{v}_1'(z)$, computed. Then in lines `11–13` the structure functions $w_1(z)$, $u_1(z)$, $h_1(z)$ and $p_1(z)$, and the constants $g_1$ and $\bar{g}_1$ are updated. Processing then passes to the next residual.

The Matlab function `ll(m)` implements $\mathcal{L}(mk_c)$ with the appropriate solvability conditions. `rc` and `kc` are $R_c$ and $k_c$ from (5). Other Matlab functions are:

`d2f(`*`arg`*`,z)` computes the second order $z$-derivative of its argument;

`dmf(`*`arg`*`,z)` computes the first order $z$-derivative of its argument midway between grid points;

`mav(`*`arg`*`,z)` computes the average of its argument midway between grid points;

`pad(`*`arg`*`,z)` pads each end of its vector argument with `NaN`.

These functions are simply specified as linear operators in REDUCE. Since REDUCE is given no rule for evaluating them, it passes the unevaluated expressions directly to the output file. The functions are then implemented in Matlab using finite differences.

This may seem a complicated procedure—many calculations are done on each iteration and higher order residuals are very complex. But in fact, the iteration converges very rapidly. After only five iterations, the maximum residual is reduced to around $5 \times 10^{-13}$ in less that five minutes!

# 5 Results and error estimates

Once the structure functions, $\mathbf{v}_l(z)$, are computed in MATLAB, the asymptotic expansions (8) and (10), truncated to some order, are assembled. These allow computation of the field variables: $u$, $w$, $\theta$ and $p$. All that needs to be specified are the values of the Rayleigh number $R$, the Prandtl number $\sigma$ and the amplitude $a$. Between them $R$ and $\sigma$ specify the nature of the fluid—viscosity, thermal diffusivity and so forth, and physical factors like the applied temperature gradient and the vertical scale of the containing walls. The evolution of the system in time is governed by the slow evolution (9) of the amplitudes, $a$ and $b$, using the computed values of $g_l$ and $\bar{g}_l$ in (10).

In this section we present some illustrative results for different models, distinguished by the order of their *truncation error*. We consider the planform evolution for a high-order model and lastly, compare the steady-state models pairwise to estimate relative errors over a region of the $(\sigma, R)$ parameter space.

## 5.1 Computed structure functions

Figure 3 shows an example of the computed vertical structure functions, all of which have the expected roughly sinusoidal shape. The advantage of computing them numerically is that they are as easy to compute for a high order term as a low order term. A sufficient number of grid points was used to obtain the coefficients to 4 decimal places.

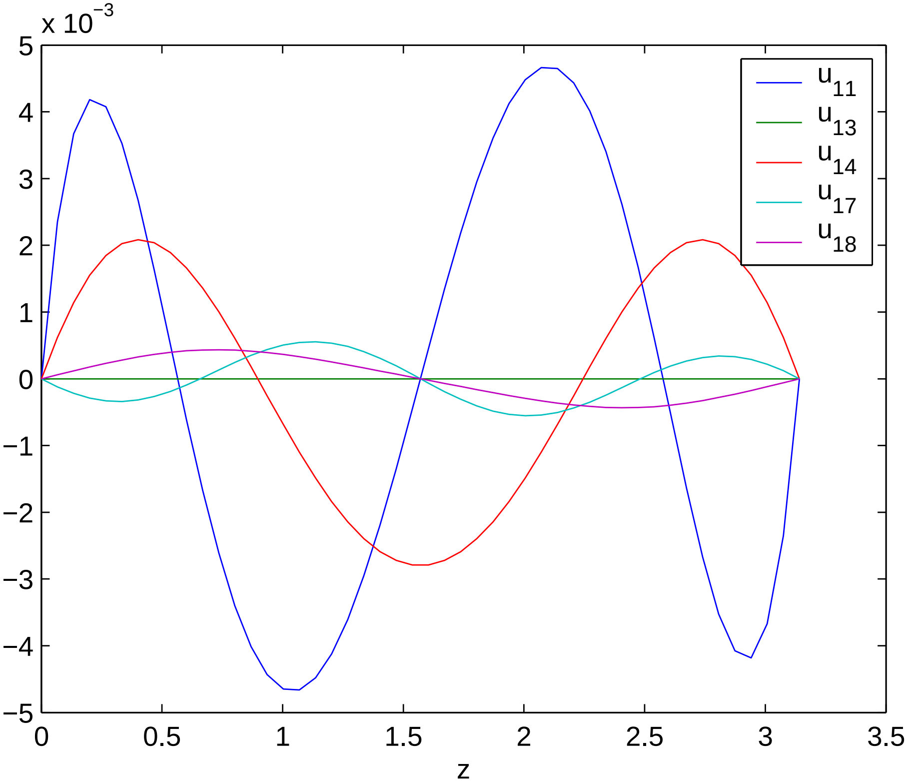

Figure 3: Computed vertical structure functions for horizontal velocity. Shown are the imaginary parts of $u_{11}$, $u_{13}$, $u_{14}$, $u_{17}$ and $u_{18}$, which represent respectively $R_d a\mathcal{E}$, $R_d ab\mathcal{E}^0$, $R_d a^2\mathcal{E}^2$, $R_d a^2 b\mathcal{E}$ and $R_d a^3\mathcal{E}^3$ terms.

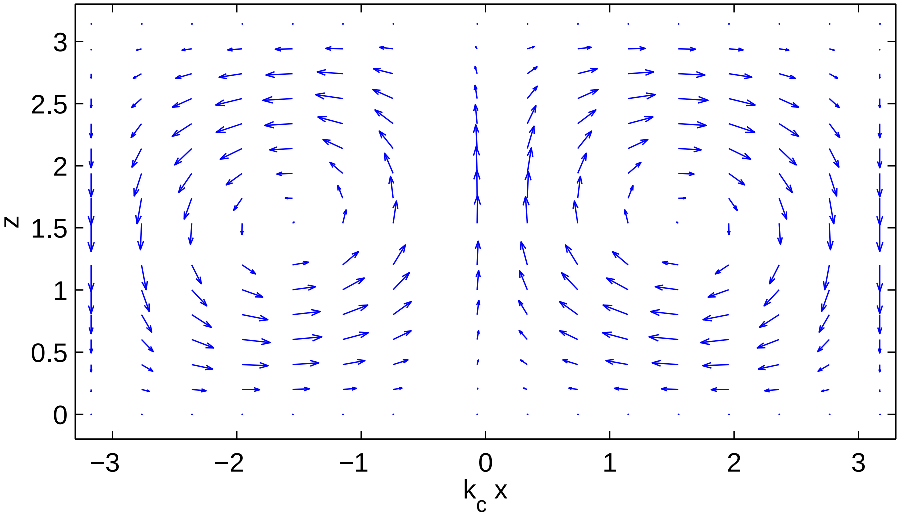

Figure 4: The velocity field for the $\mathcal{O}\left(|a|^4, R_d^2, \sigma^2\right)$ model at $R = 26$ and $\sigma = 0{\cdot}3$ . The field was computed for the steady-state amplitude predicted in (17).

## 5.2 Model flows

The lowest order model considered was $\mathcal{O}\left(|a|^4, R_d^2, \sigma^2\right)$ , which has 36 terms in its expansion. For illustrative purposes, we chose $R = 26$ and $\sigma = 0{\cdot}3$ to represent a low Prandtl number fluid above threshold. One period of the velocity field, computed for the steady-state amplitude, is shown in Figure 4.

The predicted field of temperature corrections (deviations from the hydrostatic temperature field) for the same model and parameter values is shown in Figure 5 and the pressure corrections in Figure 6.

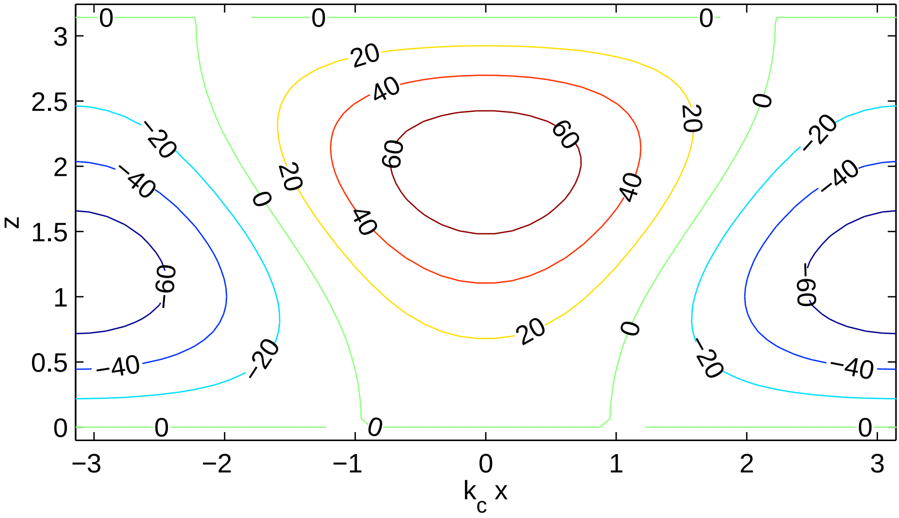

Figure 5: The temperature correction field for the $\mathcal{O}\left(|a|^4, R_d^2, \sigma^2\right)$ model at $R = 26$ and $\sigma = 0{\cdot}3$ . Note the ‘keystone’ shape of the cells as hotter fluid rises above, and cooler fluid sinks below the mid-line.

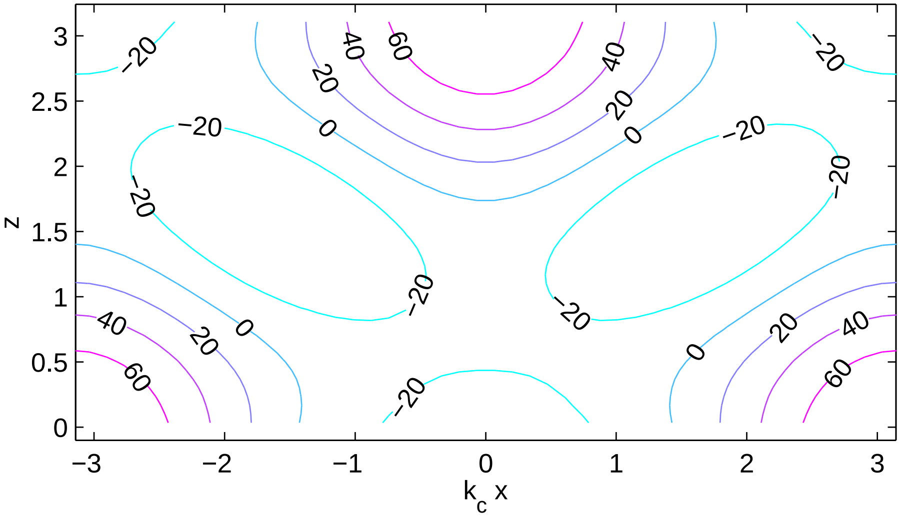

Figure 6: The pressure correction field for the $\mathcal{O}\left(|a|^4, R_d^2, \sigma^2\right)$ model at $R = 26$ and $\sigma = 0{\cdot}3$. Corrections are deviations from the hydrostatic pressure field.

## 5.3 Planform evolution and steady-state amplitude

The planform evolution computed numerically is

$$\begin{aligned}\frac{\partial a}{\partial t} &= g(a,b,R,\sigma) \qquad (16)\\ &= aR_d(0{\cdot}2214 - 0{\cdot}4334\,\sigma - 0{\cdot}0257\,R_d\sigma + 0{\cdot}8491\,\sigma^2 + 0{\cdot}1490\,R_d\sigma^2)\\ &\quad + a^2b(-0{\cdot}0162 + 0{\cdot}0409\,\sigma - 0{\cdot}0034\,R_d\sigma - 1{\cdot}4586\,\sigma^2 - 0{\cdot}0871\,R_d\sigma^2)\\ &\quad + a^3b^2(0{\cdot}0008 - 0{\cdot}0002\,R_d - 0{\cdot}0015\,\sigma + 0{\cdot}0007\,R_d\sigma - 0{\cdot}0001\,R_d^2\sigma\\ &\quad - 0{\cdot}0030\,\sigma^2 + 0{\cdot}0002\,R_d\sigma^2 + 0{\cdot}0001\,R_d^2\sigma^2) + \mathcal{O}\left(|a|^6, \sigma^3, R_d^3\right)\,.\end{aligned}$$

As expected for a supercritical bifurcation, the cubic $a^2b$ term gives nonlinear stabilisation to the linear growth term $aR_d$ and $a$ evolves quickly to a *steady-state amplitude* $a_s$.

The steady-state amplitude is found approximately by setting $\partial a/\partial t = 0$ in (16) and ignoring $a^3b^2$ terms to obtain

$$a_s \approx \sqrt{R_d\left[\frac{0{\cdot}2214 - 0{\cdot}4434\,\sigma - 0{\cdot}0257\,R_d\sigma + 0{\cdot}8491\,\sigma^2 + 0{\cdot}1490\,R_d\sigma^2}{0{\cdot}0162 - 0{\cdot}0409\,\sigma + 0{\cdot}0034\,R_d\sigma + 1{\cdot}4586\,\sigma^2 + 0{\cdot}0871\,R_d\sigma^2}\right]}\,. \qquad (17)$$

The model calculations for this paper were all done at this steady-state amplitude.

## 5.4 Model comparisons and errors

For comparison, flow fields for different order models were all calculated for the same parameter values, $R = 26$ and $\sigma = 0{\cdot}3$ . Velocity fields and temperature correction contours for $\mathcal{O}\left(|a|^6, R_d^2, \sigma^2\right)$ are shown in Figure 7, for $\mathcal{O}\left(|a|^4, R_d^3, \sigma^3\right)$ are shown in Figure 8, and those for $\mathcal{O}\left(|a|^6, R_d^3, \sigma^3\right)$ are shown in Figure 9.

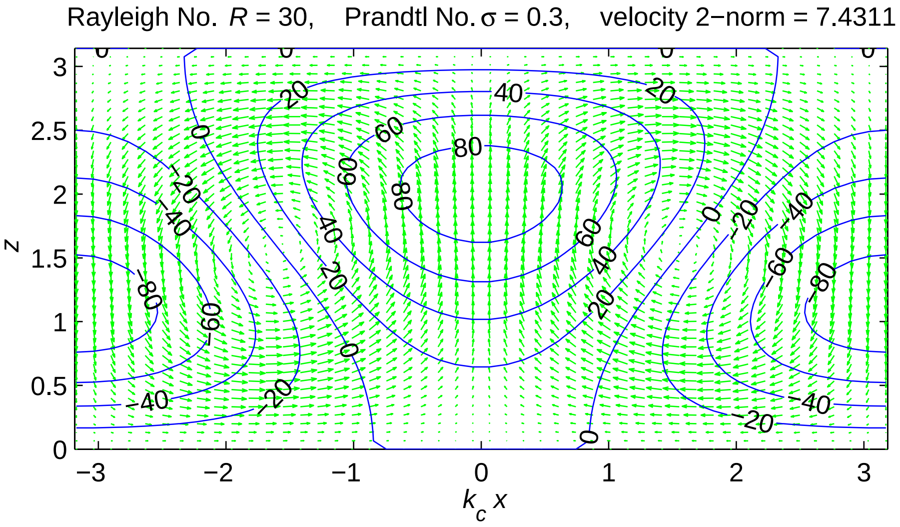

Figure 7: The velocity field (green) and temperature correction contours (blue) for the $\mathcal{O}\left(|a|^6, R_d^2, \sigma^2\right)$ model.

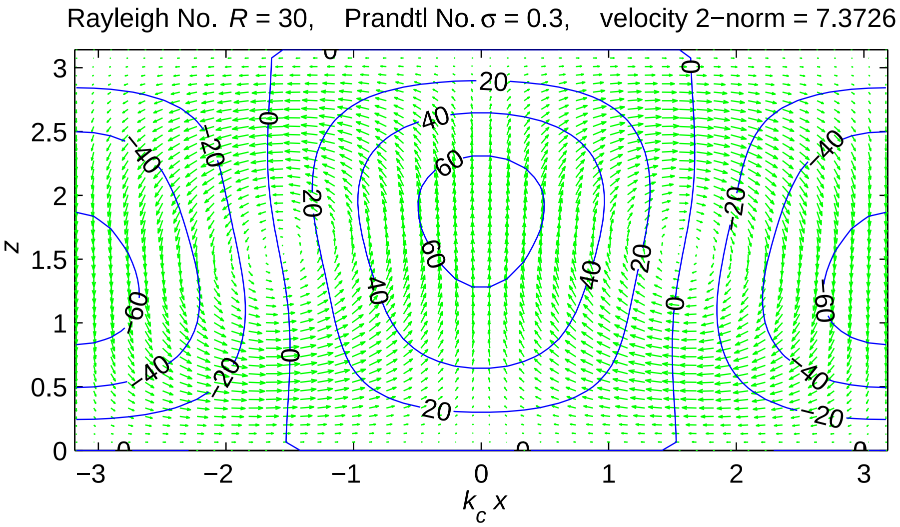

Figure 8: The velocity field (green) and temperature correction contours (blue) for the $\mathcal{O}\left(|a|^4, R_d^3, \sigma^3\right)$ model. Predicted temperature gradients are less severe than in Figure 7.

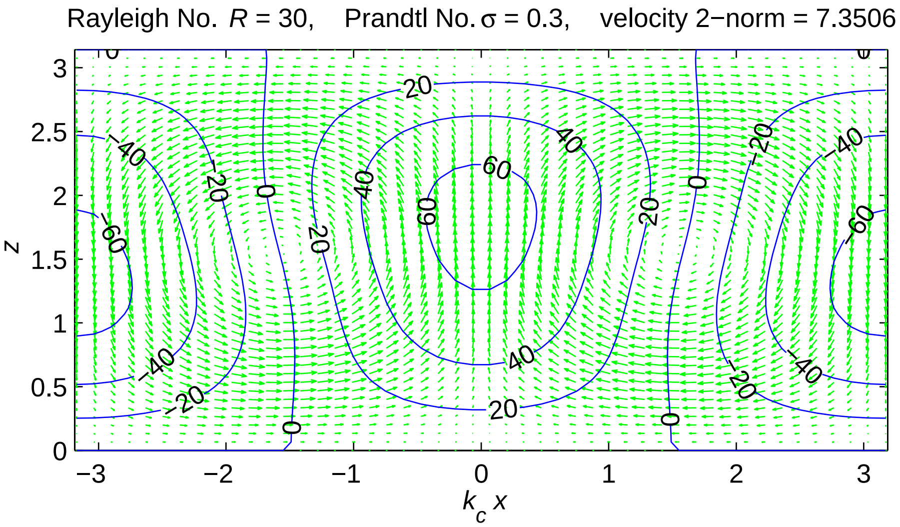

Figure 9: The velocity field (green) and temperature correction contours (blue) for the $\mathcal{O}\left(|a|^6, R_d^3, \sigma^3\right)$ model. This model is very similar to Figure 8

Comparing Figures 5 and 7, the temperature contours are very similar in moving from an $\mathcal{O}\left(|a|^4\right)$ to an $\mathcal{O}\left(|a|^6\right)$ model, so that increasing the order in $a$ has only had a subtle effect. On the other hand, compare both of these figures with Figures 8 and 9 to gauge the effect of increasing the order from $\mathcal{O}\left(R_d^2, \sigma^2\right)$ to order $\mathcal{O}\left(R_d^3, \sigma^3\right)$. There is a pronounced difference—Figures 8 and 9 predict a much less severe temperature gradient inside the rolls and consequently less of a 'keystone' effect. The predicted pressure fields show analogous effects. Thus increasing the order in $R_d$ and $\sigma$ has a major effect on the model predictions.

Lastly, we compare the performance of each the models over a whole region of the $(\sigma, R)$ parameter space. The $\mathcal{O}\left(|a|^4, R_d^3, \sigma^3\right)$ model was chosen as the basis for comparison and 1-norm relative errors for the other models computed relative to it. The $\mathcal{O}\left(|a|^4, R_d^3, \sigma^3\right)$ model is itself an approximation to the full system, with unknown error. So there is a component of error unaccounted for by this procedure. Nonetheless, the error contours in Figures 10–12 do show where different truncation error models are discrepant and where they agree well. They also gives us an idea of the useful parameter range of each model.

Figures 10–12 show 1-norm relative error contours for the velocity field. Error contours for the temperature and pressure correction fields are broadly similar to these but have a more complex structure. We use a relative error of $0{\cdot}1$ or less as an indicator of good performance. For fluids with very low Prandtl number $(0 < \sigma < 0{\cdot}08)$ all the models deteriorate in performance once the Rayleigh number gets above $R \approx 25$. For $0{\cdot}08 < \sigma < 0{\cdot}8$, the models all show good performance up to Rayleigh numbers around 35, and for $\sigma > 0{\cdot}8$, up to $R \approx 30$. The deterioration in performance for higher Rayleigh numbers is most gradual for the highest order model, $\mathcal{O}\left(|a|^6, R_d^3, \sigma^3\right)$, as the highest order model is most sensitive.

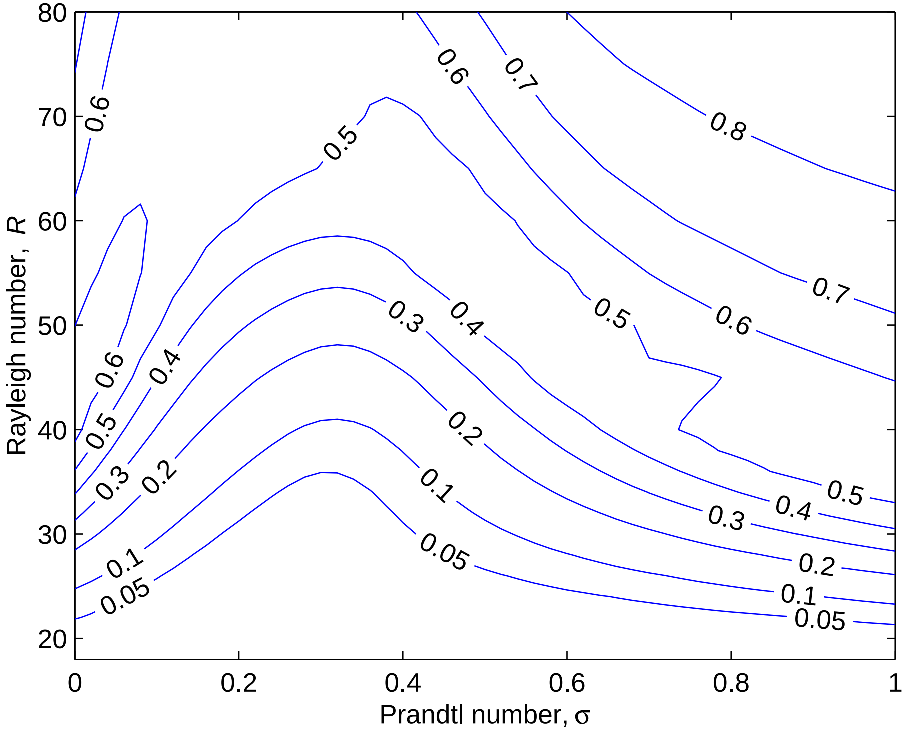

Figure 10: Relative 'error' contours for the $\mathcal{O}\left(|a|^4, R_d^2, \sigma^2\right)$ model compared to the $\mathcal{O}\left(|a|^4, R_d^3, \sigma^3\right)$ model. Contours are the 1-norm relative error in the velocity field.

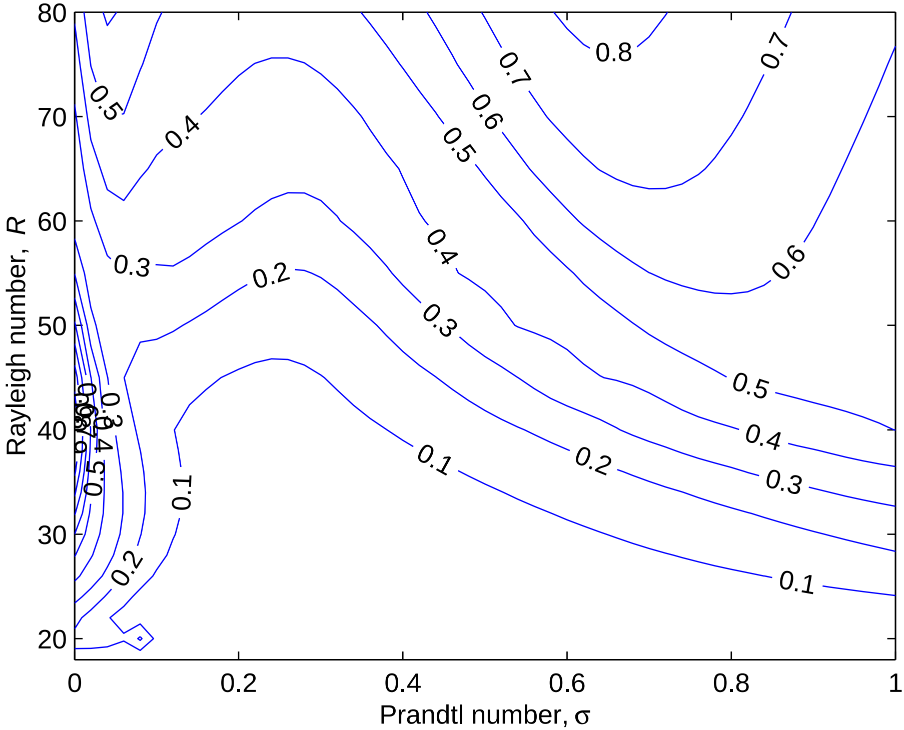

Figure 11: Relative ‘error’ contours for the $\mathcal{O}\left(|a|^6, R_d^2, \sigma^2\right)$ model compared to the $\mathcal{O}\left(|a|^4, R_d^3, \sigma^3\right)$ model. Contours are the 1-norm relative error in the velocity field.

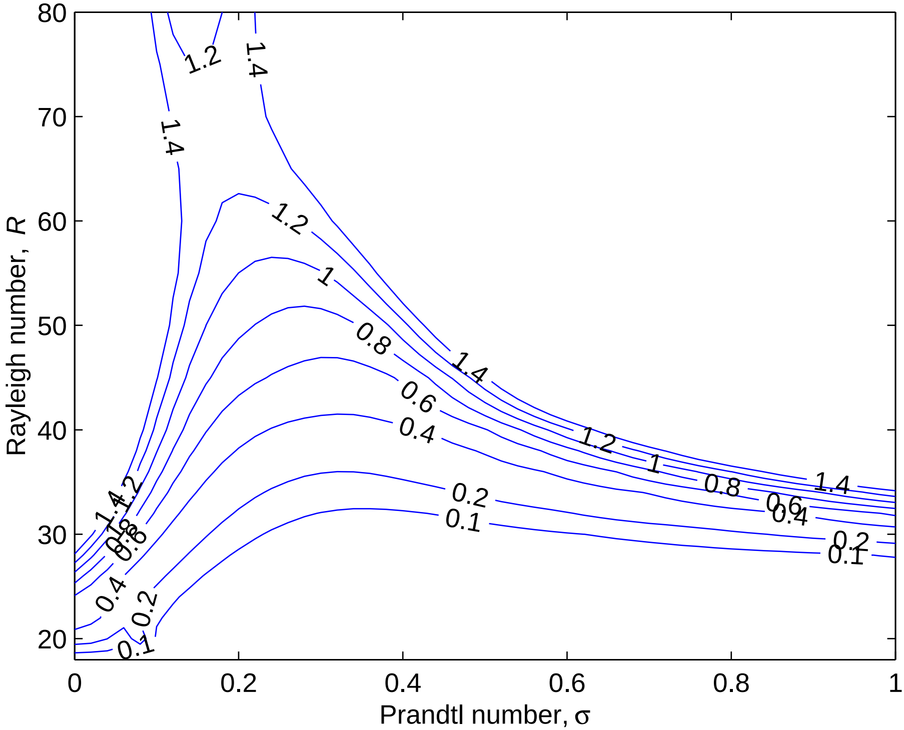

Figure 12: Relative ‘error’ contours for the $\mathcal{O}\left(|a|^6, R_d^3, \sigma^3\right)$ model compared to the $\mathcal{O}\left(|a|^4, R_d^3, \sigma^3\right)$ model. Contours are the 1-norm relative error in the velocity field.

# 6 Conclusion

The method we have outlined for computing structure functions in high-order asymptotic expansions is both efficient and robust. Though applied here to Rayleigh-Bénard convection, it is applicable to perturbation expansions generally. Only hardware limitations prevent the extension of the order of the expansions further.

We plan to use the present model to investigate the development of oscillatory instability in roll mode convection which is known to occur at low Prandtl number.

# References

[1] M. Assenheimer and V. Steinberg. Rayleigh-Bénard convection near the gas-liquid critical point. *Phys. Rev. Lett.*, 70(25):3888–3891, 1993. C593

[2] Kapil M. S. Bajaj, David S. Cannell, and Guenter Ahlers. Competition between spiral-defect chaos and rolls in Rayleigh-Bénard convection. *Phys. Rev. E*, 55(5):R4869–R4872, 1997. C594

[3] Eberhard Bodenschatz, Werner Pesch, and Guenter Ahlers. Recent developments in Rayleigh-Bénard convection. *Annu. Rev. Fluid Mech.*, 32:709–778, 2000. C592, C594, C598

[4] F. H. Busse. The oscillatory instability of convection rolls in a low Prandtl number fluid. *J. Fluid Mech.*, 52(1):97–112, 1972. C596, C597

[5] F. H. Busse. Non-linear properties of thermal convection. *Rep. Prog. Phys.*, 41:1929–1967, 1978. C593, C598

[6] Reha V. Cakmur, David A. Egolf, Brendan B. Plapp, and Eberhard Bodenschatz. Bistability and competition of spatiotemporal chaotic and fixed point attractors in Rayleigh-Bénard convection. *Phys. Rev. Lett.*, 79(10):1853–1856, September 1997. C594

[7] Jack Carr. *Applications of Centre Manifold Theory*, volume 35 of *Applied Mathematical Sciences*. New York: Springer-Verlag, 1981. C600

[8] R. M. Clever and F. H. Busse. Transition to time-dependent convection. *J. Fluid Mech.*, 65:625–645, 1974. C592

[9] Vincent Croquette and Hugh Williams. Nonlinear competition between waves on convective rolls. *Phys. Rev. A*, 39(5):2765–2768, March 1989. C593

[10] M. C. Cross and P. C. Hohenberg. Pattern formation outside of equilibrium. *Reviews of Modern Physics*, 65(3):851–1112, July 1993. C592

[11] J. R. de Bruyn, E. Bodenschatz, S. W. Morris, S. P. Trainoff, Y. Hu, et al. Apparatus for the study of Rayleigh-Bénard convection in gases under pressure. *Rev. Sci. Inst.*, 67(6):2043–2067, 1996. C594

[12] L. E. Howle. A comparison of the reduced Galerkin and pseudo-spectral methods for simulation of steady Rayleigh-Bénard convection. *Int. J. Heat Mass Transfer*, 39(12):2401–2407, 1996. C592

[13] P. Laure and Y. Demay. Symbolic computation and equation on the center manifold: application to the Couette-Taylor problem. *Computers & Fluids*, 16(3):229–238, 1988. C607

[14] J. Liu and G. Ahlers. Spiral-defect chaos in Rayleigh-Bénard convection with small Prandtl numbers. *Phys. Rev. Lett.*, 77(15):3126–3129, 1996. C594

[15] Paul Manneville. *Dissipative Structures and Weak Turbulence.* Perspectives In Physics. San Diego: Academic Press, 1990. C595, C596, C598, C599

[16] S. W. Morris, E. Bodenschatz, D. S. Cannell, and G. Ahlers. Spiral defect chaos in large aspect ratio Rayleigh-Bénard convection. *Phys. Rev. Lett.*, 71(13):2026–2029, 1993. C593, C594

[17] Stephen W. Morris, Eberhard Bodenschatz, David S. Cannell, and Guenter Ahlers. The spatio-temporal structure of spiral-defect chaos. *Physica D*, 97:164–179, 1996. C594

[18] Alan C. Newell and J. Whitehead. Finite bandwidth, finite amplitude convection. *J. Fluid Mech.*, 38:279–303, 1969. C600

[19] Rayleigh, Lord. On convective currents in a horizontal layer of fluid when the higher temperature is on the under side. *Philosophical Magazine*, 32(6):529–546, 1916. C593

[20] A. J. Roberts. The application of centre-manifold theory to the evolution of systems which vary slowly in space. *J. Austral. Maths. Soc. B*, 29:480–500, 1988. C592, C600

[21] A. J. Roberts. Planform evolution in convection—an embedded centre manifold. *J. Austral. Maths. Soc. B*, 34:174–198, 1992. C592, C600

[22] Lee A. Segel. Distant side-walls cause slow amplitude modulation of cellular convection. *J. Fluid Mech.*, 38(1):203–224, 1969. C600

[23] Eric D. Siggia and Annette Zippelius. Pattern selection in Rayleigh-Bénard convection near threshold. *Phys. Rev. Lett.*, 47(12):835–838, September 1981. C594